Nanoscale

ROYAL SOCIETY OF CHEMISTRY

PAPER

View Article Online
View Journal | View Issue

Check for updates

Cite this: *Nanoscale*, 2021, **13**, 7308

Hydrogenation of diamond nanowire surfaces for effective electrostatic charge storage†

Kalpataru Panda, *[a,b] Jae-Eun Kim, [a] Kamatchi Jothiramalingam Sankaran,[c,d] I-Nan Lin,[e] Ken Haenen, [c,d] Georg S. Duesberg [b] and Jeong Young Park *[a,f]

We report a novel versatile method for writing charged areas on diamond nanowire (DNW) surfaces using an atomic force microscopy (AFM) tip. Transmission electron microscopy (TEM) investigations revealed the existence of abundant plate-like diamond aggregates, which were encased in layers of graphite, forming nano-sized diamond-graphite composites (DGCs) on DNW surfaces. These DGCs are the main feature, acting as charge-trapping centers and storing electrostatic charge. A hydrogenation process has been observed effectively enhancing the charge-trapping properties of these DNW materials. The effective charge trapping properties with hydrogenation are ascribed to the disintegration of the DGCs into smaller pieces, with an overall increase in the metallic nanographitic phase fractions in a dielectric diamond matrix. Moreover, the written charge on the surface can be easily modified, re-written, or completely erased, enabling application in diamond-based re-writable electronic devices. However, excessive hydrogenation degrades the charge-trapping properties, which is attributed to the etching of the DGCs from the surface. This study demonstrates the potential importance of a simple hydrogenation process in effective electrostatic charge trapping and storage for diamond related nanocarbon materials and the role of DGCs to further enhance it.

Received 11th January 2021,
Accepted 12th March 2021

DOI: 10.1039/d1nr00189b

rsc.li/nanoscale

1. Introduction

The manipulation and storage of electrostatic charge are currently a main concern in the field of nanoscience because of their direct applicability toward energy harvesting.[1–4] The electrostatic charging concept is used for wetting plastics for painting, printers and copiers for toner positioning on paper,[5] memory devices, the manipulation of transport properties of field-effect transistors,[6] and the self-assembly of micro and nanosized particles on insulating materials.[7] The basic elementary processes, such as the control over the electrostatic charge, electrification techniques, and solution for the effective charge relaxation techniques, can be successfully explained by properly understanding the nature of electrostatic charging. Different methods, such as focused ion beam,[8] electron beam,[9] nanoimprinting[10] and soft lithography-based techniques,[11–18] have been adopted for sequential charge writing. However, the techniques mentioned above are costly and time consuming, and require a master template for further processing.[17,18] Electrostatic charge writing using an AFM tip is simpler and more cost-effective.

Charge injection into dielectric materials by contact electrification is also of great scientific interest for developing devices, including triboelectric nanogenerators for building self-powered portable electronic devices, large-scale energy harvesting, and data storage devices.[19] This effect has also been utilized for a variety of other purposes (*e.g.*, painting,[20,21] particle separation,[22] and mechanical energy harvesting[23,24]). All these processes use contact electrification-induced charges (*i.e.* tribo–charges) as the source to generate electricity from mechanical energy *via* impact,[25] sliding,[26,27] and rotation.[28] For better performance, transferring and sustaining a higher density of charges on the surface during the contact electrification process is always favourable.[29] Therefore, control of the

---

[a] Department of Chemistry, Korea Advanced Institute of Science and Technology (KAIST), Daejeon, 34141, South Korea. E-mail: phy.kalpa@gmail.com, kalpataru.panda@unibw.de
[b] Institute of Physics, EIT 2, Faculty of Electrical Engineering and Information Technology, Universität der Bundeswehr München, Werner-Heisenberg-Weg 39, 85577 Neubiberg, Germany
[c] Institute for Materials Research (IMO), Hasselt University, 3590 Diepenbeek, Belgium
[d] IMOMEC, IMEC vzw, 3590 Diepenbeek, Belgium
[e] Department of Physics, Tamkang University, 251 Tamsui, Taiwan, Republic of China
[f] Center for Nanomaterials and Chemical Reactions, Institute for Basic Science (IBS), Daejeon, 34141, South Korea. E-mail: jeongypark@kaist.ac.kr

† Electronic supplementary information (ESI) available: High resolution XPS spectra of pristine DNW_0 and hydrogenated DNW surfaces; table showing the relative intensities of various components of the C 1s XPS spectra from the pristine DNW_0 and the H_2 plasma-treated DNW surfaces. FESEM morphology of the diamond-coated tip before and after the load dependent/high bias experiments; charge writing and erasing processes by AFM on the DNW_0 surface. See DOI: 10.1039/d1nr00189b

contact electrification induced charge is a serious subject. Previously, the modulation of contact electric charge density was realized through intrinsic approaches, such as material selection, that directly change the structure of the two surfaces that are in contact.[30] Surface modification and functionalisation is an important method, as it can control the contact electrification induced charge; however, studies on the relation of surface modification induced electrification charge are limited.

Recent research on portable electronic devices has attracted much interest because of their easy mobility, low cost, and greater storage capacity compared to conventional storage devices.[31] Different materials, *e.g.* semiconductors, polymers, electrets and waxes, were used for charge storage flash memory devices.[32–35] Besides these, other materials, such as amorphous silicon,[36] polytetrafluoroethylene, and poly methyl methacrylate,[37,38] have already been used for electrostatic charge trapping purposes. Exploring a better charge-trapping material and subsequently analyzing its local charge-trapping properties are necessary for further improving the efficiency of electronic devices. Although charge storage in oxide/insulating materials has gained attention, it still presents a great scientific challenge, due to a deficit of knowledge of the specific mechanisms related to the generation, transport, and storage of charges. Diamond could be an interesting material for use as an electrostatic charge-trapping material because of its unique set of interesting electronic properties.[39–41] Perceiving, finding, and enhancing the basic electrostatic charging properties of diamond are important for diamond-based electronic device applications.

This paper addresses the electrostatic charge-trapping properties of one-dimensional diamond nanowire (DNW) films, synthesized by the microwave plasma enhanced chemical vapor deposition, subjected to hydrogen plasma treatments. Short hydrogenation treatments to DNWs are observed to effectively enhance charge-trapping properties; however an extended hydrogenation period degrades them. The possible mechanism for the enhanced charge-trapping properties of hydrogenated DNWs is discussed.

2. Experimental

700 nm thick DNW films were deposited on n-type silicon (100) substrates with N_2 (94%)/CH_4 (6%) plasma by microwave plasma-enhanced chemical vapor deposition (MPECVD). After the deposition, they were post-treated with H_2 plasma for 5, 10 and 15 minutes at a pressure of 7 mbar with a microwave power of 600 W. For clarity, the 5, 10 and 15-minute hydrogen plasma treated films were designated as "DNW_5", "DNW_{10}", and "DNW_{15}", respectively; the pristine DNW films were designated as "DNW_0". The morphological and microstructural characterization of these films was performed using a FESEM (JEOL 6500) and a TEM (JEOL 2100, 200 eV), respectively. The bonding structures were evaluated using Raman spectroscopy (Lab Raman HR800, Jobin Yvon) at an excitation wavelength of 632.8 nm, XPS (PHI 1600) at room temperature and EELS (Gatan Enfina in TEM).

A multi-mode VIII AFM was used for the local electrostatic charge writing and patterning purposes under ambient conditions. For Kelvin probe force microscopy (KPFM) experiments, the Si substrate bases of the DNW film were pasted to a steel disc using a conductive silver paint. Conductive diamond-coated silicon probes (diamond doped with nitrogen for conductivity, DCP11 by NT-MDT) were used for the AFM experiments. The tip height and radius of curvature were 10–15 μm and ~100 nm, respectively. The DNW/silicon substrates were grounded while the bias voltage was applied to the AFM tip. The voltages applied to the tip ranged from +10 to −10 V. The KPFM technique was used to detect the contact potential difference (CPD) between the written and unwritten charged areas on the DNW surfaces. All the charge-writing experiments were performed under ambient conditions, *i.e.* the relative humidity and temperature were within 20–30% and 22–25 °C, respectively. Using a similar procedure, all the charge patterns were written with the same tip on different areas of the DNW surface.

3. Results and discussion

3.1 Surface morphology and chemical properties of pristine and hydrogenated DNW films

Plane-view field emission scanning electron microscopy (FESEM) micrographs of pristine and hydrogenated DNW films with the enlarged view in the respective insets are shown in Fig. 1. Pristine DNW films (DNW_0, Fig. 1a) possess a dense wire-like granular structure (lengths and widths varying from 0.2–1 μm and 5–10 nm, respectively) that is evenly distributed over the entire sample surface. Hydrogenation for 5 min (Fig. 1b, DNW_5) starts to break the wire-like structure of the DNWs into shorter lengths. Moreover, at 10 min of hydrogenation (Fig. 1c, DNW_{10}), the DNWs become still shorter with a wider wire-like structure. The grains of the DNW films become still finer and no more wire-like structure is observed in the extended 15 min hydrogenation period (DNW_{15}, Fig. 1d). The detailed microstructural analysis is carried out by TEM, described shortly.

Structural changes caused by the hydrogenation process were examined *via* Raman spectroscopy (Fig. 1e). A broad peak at around 1120 cm^{-1} is the *trans*-polyacetylene (TPA) phase, marked in Fig. 1e for the DNW_0, DNW_5, DNW_{10} and DNW_{15} films.[42–45] The D* band and G band at around 1334 cm^{-1} and 1594 cm^{-1} represent the disordered carbon and graphitic nature of the DNW_0, DNW_5, DNW_{10} and DNW_{15} films (Fig. 1e). The Raman spectra of the pristine (DNW_0) and hydrogenated DNW films (*i.e.*, DNW_5, DNW_{10} and DNW_{15}) in spectra i, ii, iii, and iv in Fig. 1e show that the diamond nature of these films is preserved, despite the rigorous hydrogenation process.[46] XPS measurements were carried out to more precisely understand the hydrogenation effect on the chemical bonding structure of these DNW films. The C 1s photoemission spectra of

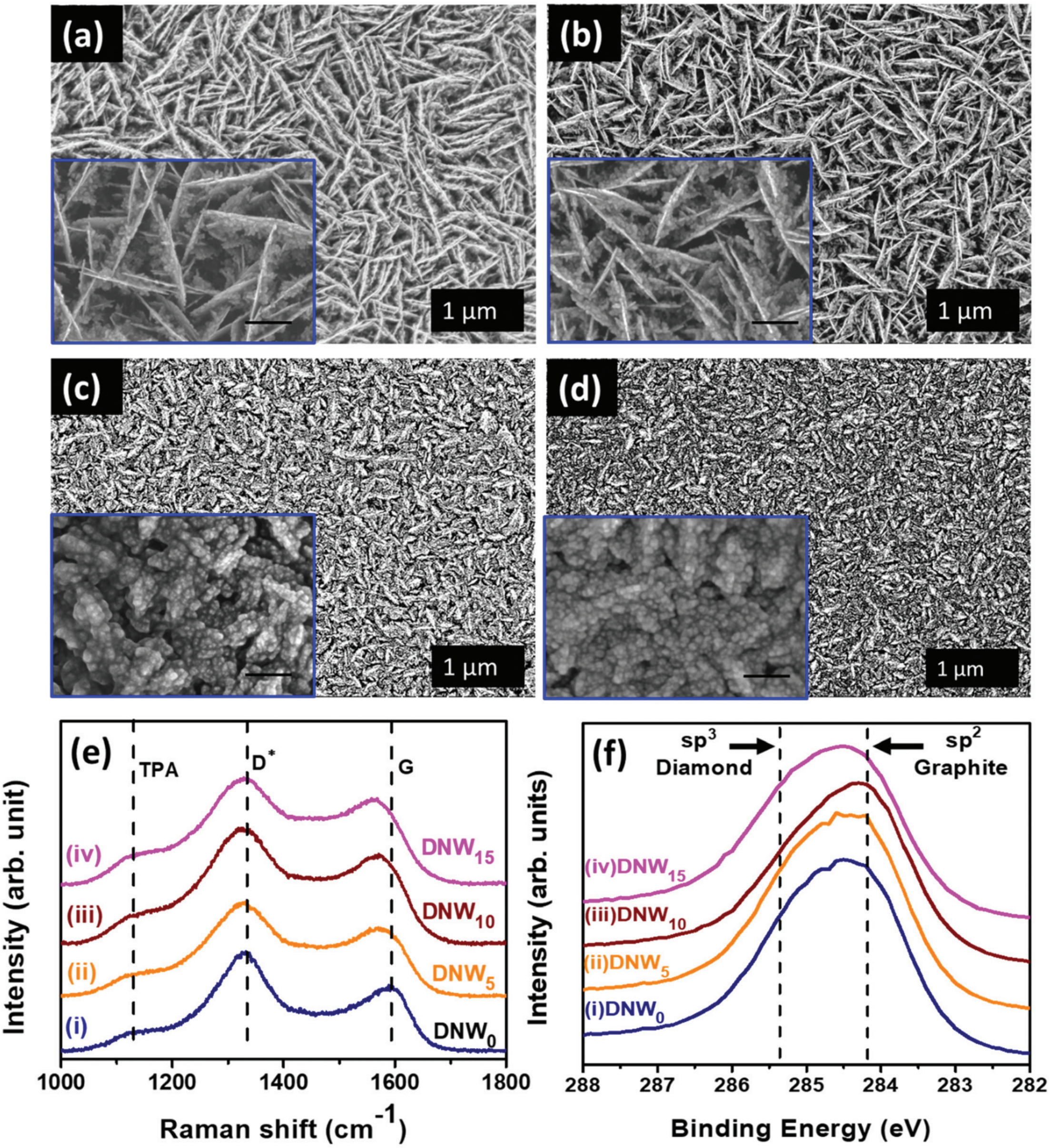

Fig. 1 Morphological and chemical characterization of pristine and hydrogenated DNW materials. FESEM surface morphology of (a) DNW$_0$ and (b–d) hydrogenated DNW films for (b) 5 min (DNW$_5$), (c) 10 min (DNW$_{10}$), and (d) 15 min (DNW$_{15}$). Insets show the enlarged view with scale bar (a and b) 200 nm and (c and d) 100 nm. (e) Raman and (f) XPS spectra of (e) pristine DNW$_0$ (spectrum i) and spectrum (ii–iv) hydrogenated films (ii) DNW$_5$, (iii) DNW$_{10}$, and (iv) DNW$_{15}$.

the pristine and hydrogenated DNW films are shown in Fig. 1f. For better clarity and to clearly record the shift in the C 1s peak, the raw data are shown. The C 1s peak position in the diamond is 285.2 eV (*i.e.*, C–C sp^3 peak position), which is about 1.1 eV higher than that in graphite (*i.e.*, 284.1 eV, C═C sp^2 peak position).[47–50] The C 1s peak position shifted towards a lower binding energy (graphitic phase) as the plasma treatment time increased from 5 min (DNW$_5$, Fig. 1f spectrum ii) to 10 min (DNW$_{10}$, Fig. 1f spectrum iii), in comparison with the pristine DNW film (DNW$_0$, Fig. 1f spectrum i). This indicates that the fraction of the sp^2 graphitic phase is higher in DNW$_{10}$ materials than in DNW$_5$ and DNW$_0$ materials. Furthermore, the fitted C 1s curve with the relative percentages of sp^2, sp^3, and C═N phase fractions in Fig. S1 and Table 1 in the ESI† clearly supports this fact. However, the extended hydrogenation period etches the sp^2 graphitic phase and the C 1s peak shifts towards a higher binding energy side (*i.e.* diamond), as seen in Fig. 1f spectrum iv for the DNW$_{15}$ films. Briefly, as discussed in Fig. S1† and Fig. 1f, an increase in the sp^2 graphitic phase fraction caused by the hydrogenation process is observed (*i.e.*, the sp^2 C═C phase fraction of 40.9% for the DNW$_0$ increases to 48.1% for the DNW$_5$ (Fig. S1,† spectrum ii) and 63.9% for the DNW$_{10}$ (Fig. S1,† spectrum iii)). However, the extended hydrogenation process (Fig. S1,† spectrum iv) etched out the graphitic phase content from the DNW_{15} surfaces, decreasing the sp^2 C═C phase fractions to 35.9%.

3.2 Charge writing on the DNW surface

An AFM tip was used to inject charges into the DNW surfaces under ambient conditions.[51] The AFM charge writing/patterning technique has several advantages over other techniques: it does not require sophisticated lithographic masks, there is no fear of radiation-induced damage, and it takes significantly less time (a few seconds to a few minutes, depending on the charge-writing shape and structure). The charge-writing procedure on the DNW material can be performed in either contact or tapping mode, as shown in the schematic in Fig. 2a. During contact mode, the tip of the AFM physically rubs the diamond surface, whereas in tapping mode, the tip taps the surface at regular intervals with the load varying from a few nN to a few N. Just after the charge-writing procedure, the CPD of the charge-written area was measured. Amplitude modulated KPFM was utilized to measure the CPD by lifting the tip to a certain defined lift height (h) above the written area, as shown in the schematic in Fig. 2b.[52–55]

Fig. 2c shows a typical AFM surface topography of the DNW_0 surface. The marked black square areas (500×500 nm^2) in the inset of Fig. 2c show the charge-writing regions where the tip bias was alternatively switched between −1 V and +1 V. After the charge-writing procedure, the CPD between the tip and the DNW surface was recorded using the KPFM mode. Fig. 2d shows the KPFM potential signal of the written area with a tip bias of +1 V. Similarly, the charge was written with a −1 V tip bias on the DNW_0 surface. Both the positive and negative charges with different shapes and sizes down to the nm scale can be patterned by varying the tip bias. The KPFM potential contrast in Fig. 2e corresponding to the written area in Fig. 2c shows that both positive and negative charges can be written on the DNW surface by switching the tip polarity. Notably, the KPFM surface potential is the CPD between the tip and the sample surface, which shows the extra charge on the sample surface.[56–58]

To investigate the hydrogenation effect on the charge-trapping properties of the DNW materials, charge-writing and subsequent charge-reading experiments were performed for the DNW_0, DNW_5, DNW_{10} and DNW_{15} materials. The surface topography with the charge writing area (shown in the middle of each figure) for the DNW_5, DNW_{10} and DNW_{15} films is shown in Fig. 3a, d and g. The corresponding CPD maps are shown in Fig. 3b, e and h, respectively. The line profile drawn through the CPD map indicated in Fig. 3b, e and h is shown in Fig. 3c, f and i, respectively. These line profiles show the extra accumulated charge trapped on the written area caused by the hydrogenation process. The accumulated charge on the DNW_0 materials increased from 80 mV (Fig. 2d) to 162 mV for DNW_5 (Fig. 3b). A further increase in the H_2 plasma treatment period again enhanced the accumulated trapped charge to 379 mV, as seen in Fig. 3e. However, further treatment degrades the charge accumulation to 112 mV, as shown in Fig. 3h for the DNW_{15}.

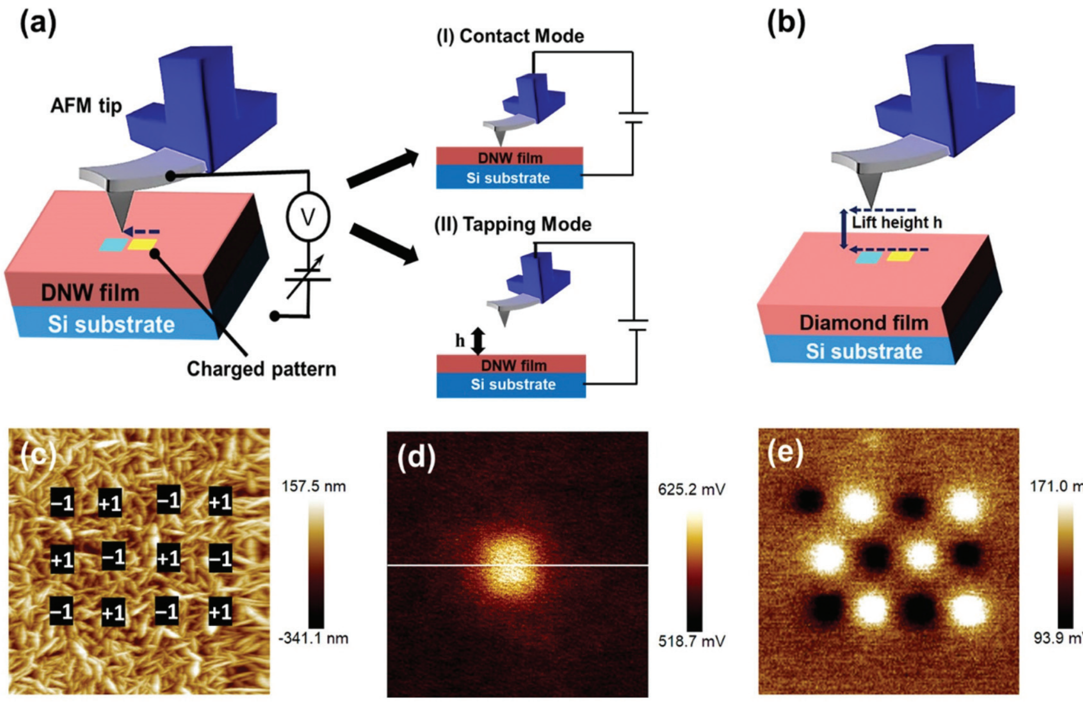

Fig. 2 Illustration of the charge writing process (a) AFM tip in (I) contact and (II) tapping mode and (b) KPFM surface imaging just after the charge writing process on the same location. (c) Charge writing on the defined regions of the DNW_0 surface by successively altering the tip polarity. Charge reading by KPFM depicting the potential on the DNW_0 surface (d) using a biased AFM tip at +1 V and (e) charge imaging of the previously written area in (c). Image sizes: (c and e) 10 μm^2; (d) 4 μm^2.

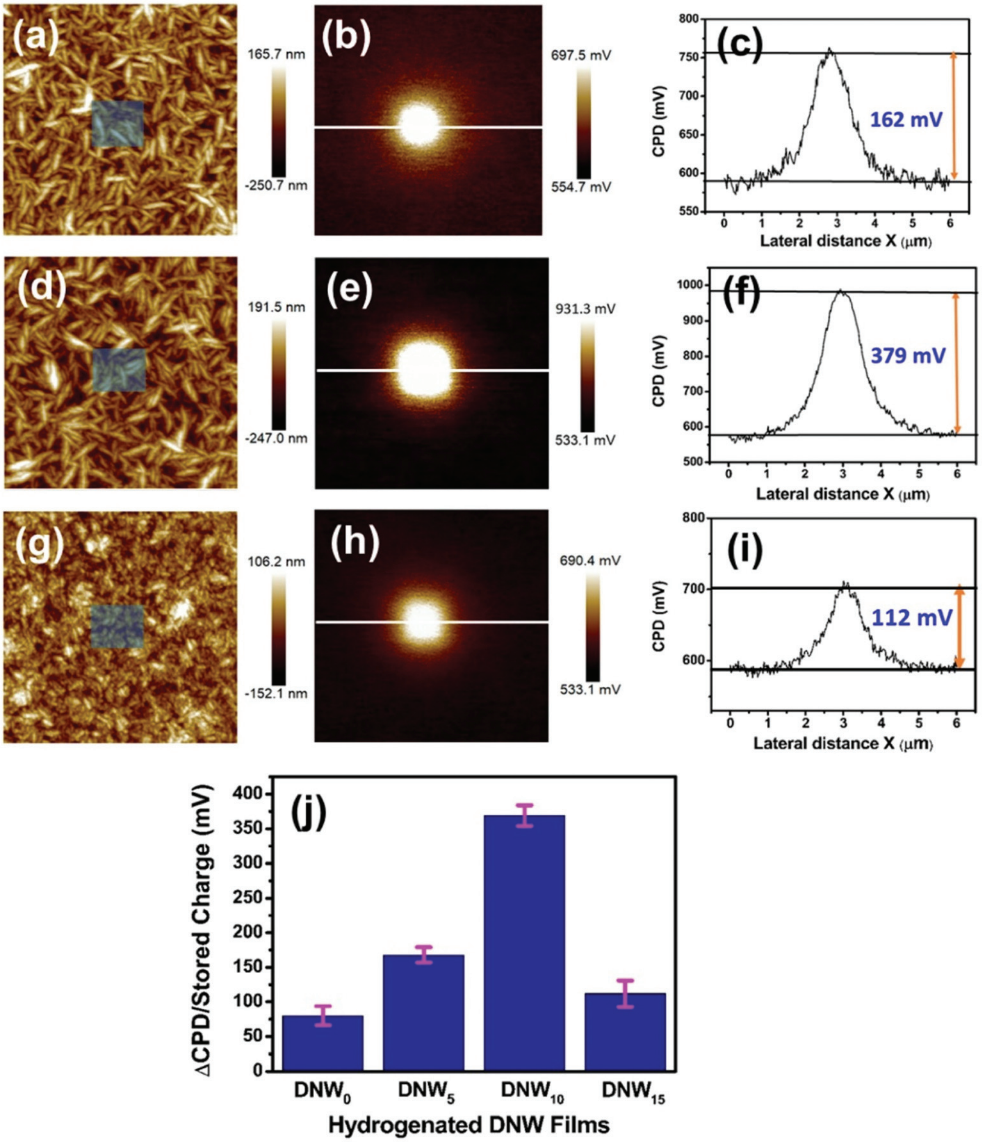

Fig. 3 Effect of the hydrogenation process on the charge trapping properties of DNW materials. AFM surface morphology of (a) DNW_5, (d) DNW_{10}, and (g) DNW_{15} films. The marked inset in the corresponding AFM surface morphology shows the area written by the AFM tip. The respective surface potential on the written area for (b) DNW_5, (e) DNW_{10}, and (h) DNW_{15} surfaces. The potentials across the line shown in (b), (e), and (h) are shown in (c), (f), and (i) for the DNW_5, DNW_{10}, and DNW_{15} films, respectively. (j) Charge storage on the DNW materials with the hydrogenation period, calculated from their corresponding potential mapping. Image sizes: (a, b, d, e, g, and h) 4 μm.

Moreover, the stability of the accumulated trapped charges in these DNW materials is a vital aspect for any real electronic applications of these materials. The trapped charge on the DNW_{10} material was monitored successively by measuring the variations in the KPFM contrast between the written area and un-written area for 480 minutes, as shown in Fig. 4. The white and grey boxes in Fig. 4a represent the writing area when the surface was scanned at tip biases of +1 and −1 V, respectively. Fig. 4b–i show the subsequent KPFM potential variations for both the positive and negative charges measured for 480 min at 60 min intervals. The variations in the KPFM potential contrast in Fig. 4b–i reveal that both the positive and negative KPFM contrasts become faint with time. It indicates the dissipation of the stored charge on the DNW_{10} surface as time passes. It was also observed that the potential contrast of the positive charge (white potential contrast in Fig. 4b–i) decays faster than that of the negative charge (black potential contrast in Fig. 4b–i), which requires further study. The dissipation of the stored charges (shown in Fig. 4j) suggests that they are stable (measured for 480 min) on the surface and dissipate slowly with time.[59–61]

The stored charge on the hydrogenated DNW materials depends on the load applied on it. As the load is increased during the charge writing procedure, the stored charge is subsequently enhanced. Fig. 5 shows the charge storage on the DNW_{10} materials with respect to the varying load. The surface of the DNW_{10} materials on which loads from 10 to 70 nN are

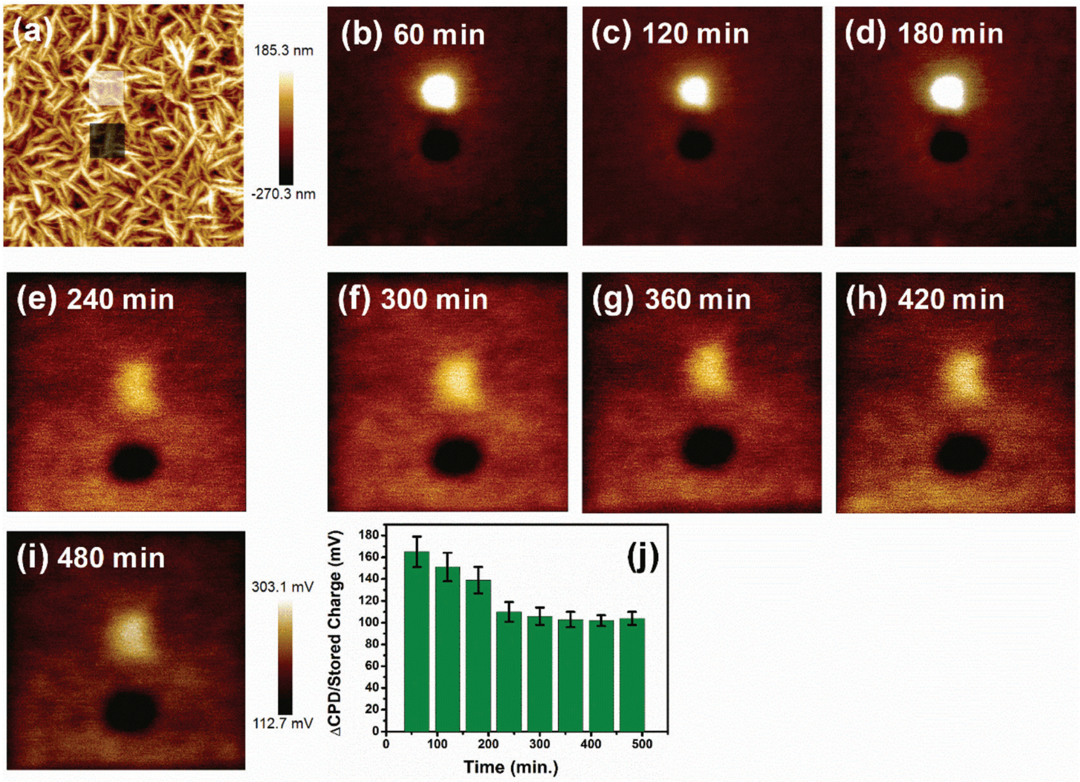

Fig. 4 The dissipation of trapped charge with time (a) AFM image of the DNW_{10} surface with the marked charge written areas, as indicated in the square boxes. (b–i) After the charge writing procedure, the KPFM signals were monitored for 480 min at 60 min intervals. (j) Time dependent dissipation of the stored charge calculated from the respective KPFM signals. Image sizes: (a–i) 6 μm.

applied with tip biases of ±1 V is shown in Fig. 5a. As the load on the surface is gradually increased, the corresponding surface potential also increases (Fig. 5b and c), which indicates the presence of effective charge on the surface. Both positive and negative charges on the surface are enhanced by increasing the loads at both positive and negative tip biases, respectively. The enhanced charge (both positive and negative) with increasing load on the surface is shown in Fig. 5d and e. Furthermore, the stored charge of these DNW_{10} materials proportionally depends on the tip bias (*i.e.*, charge injected into DNW_{10}), which is not shown here.

It should be noted that almost no change in the tip shape and size was noticed just before and after the load-dependent or high tip bias experiments, as shown in Fig. S2.† Thus, excess charge trapping by an unexpected increase in the shape and size of the tip can be disregarded.[62] Interestingly, the potential pattern that has been written on the DNW_{10} surface can be brought back to its original pristine condition by applying the same bias with reverse polarity. This indicates that DNW_{10} materials are rewritable, as shown in Fig. S3,† which could be helpful for DNW-based rewritable electronic devices.

3.3 Microstructural characterization by transmission electron microscopy

While Raman and XPS measurements reveal the change in the chemical structure of the pristine DNW films caused by the hydrogenation process, TEM measurements were carried out to reveal the microstructural change of the DNW films, which significantly affects the charge-trapping/storing properties. A typical bright field (BF) TEM micrograph of the DNW_0 films (Fig. 6a) shows uniformly distributed wire-like aggregates with lengths varying from 50 to 200 nm and diameters of a few nanometers for the pristine DNW films. The selected area electron diffraction (SAED) pattern corresponding to the TEM of the DNW_0 film, shown in the inset of Fig. 6a, exhibits ring-shaped patterns, implying the presence of random orientation of the diamond aggregates in the DNWs. The calculated lattice plane spacings corresponding to the SAED pattern of the (311), (220), and (111) planes are estimated to be 0.11, 0.12, and 0.21 nm, respectively, which are the same as those for the crystalline diamond. The central diffuse ring indicated that the matrix is of amorphous carbon. A core–shell microstructure is observed in the high-resolution TEM (HRTEM) image for the wire-like aggregates of the DNW_0 films shown in Fig. 6b. The diamond nanostructure in the DNW is encased by atomic layers with a lattice spacing of 0.34 nm and a graphitic phase of about 4 nm in thickness, while the core of the diamond nanostructure in the DNWs consists of (111) diamond lattice planes with a lattice spacing of 0.21 nm. Fourier transform (FT) patterns on the selective areas were recorded to further confirm the diamond and graphitic nanostructures. The FT diffractogram (FT image) marked in region 1 in the inset of

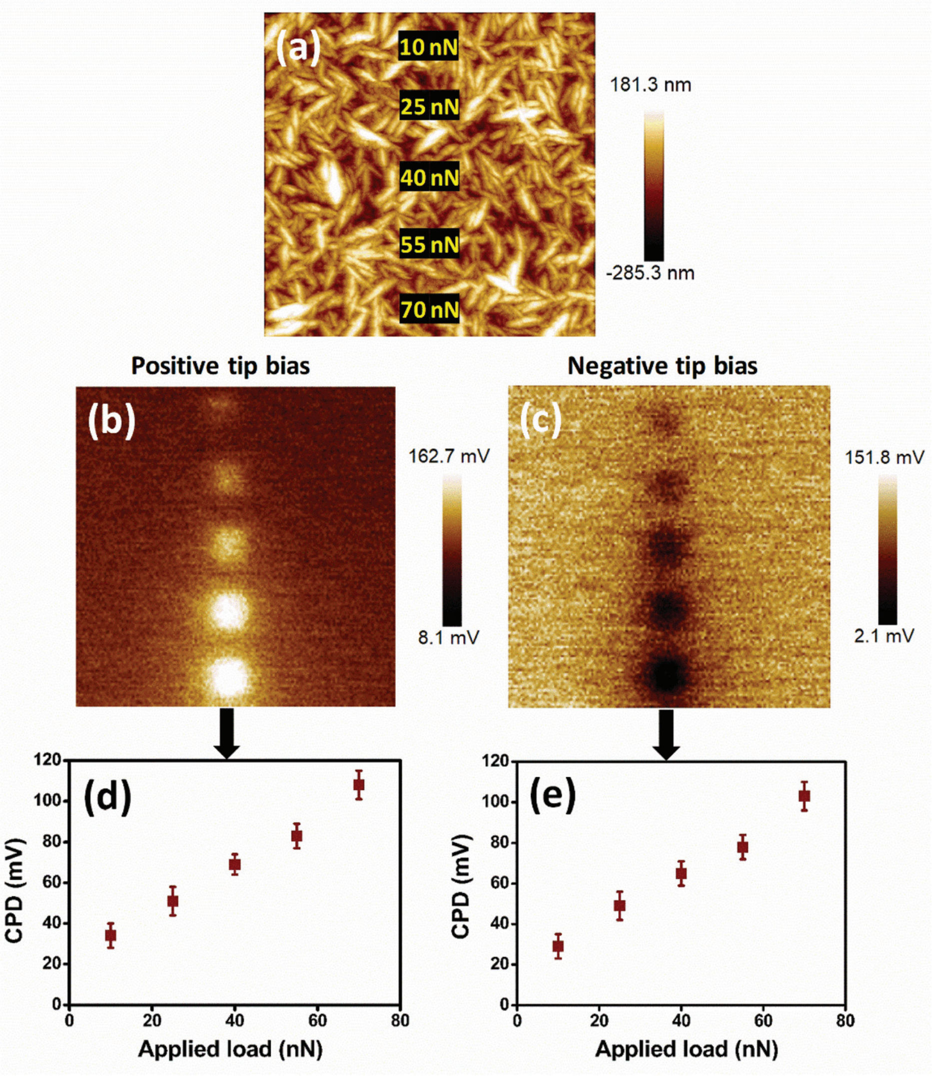

Fig. 5 Load dependent charge trapping properties of hydrogenated DNW surfaces (a) AFM image of DNW_{10} surface with the inset marked load positions where charges are written by the AFM tip. The KPFM potential signal shows the charge trapping on the surface as a function of load at a (b) positive or (c) negative tip bias. (d) Positive and (e) negative contact potential difference extracted from the respective KPFM surface potentials in (b) and (c), respectively. Image sizes: (a, b, and c) 10 μm.

the HRTEM image in Fig. 6b corresponds to diamond, whereas the nanographitic phase is observed along the shell of the DNW, as marked in region 2. Moreover, a large proportion of non-crystalline carbon phases are present in the vicinity regions as matrix. The presence of a mixture of diamond and a-C phase in the matrix of DNW_0 is illustrated in region 3 and the inset FT_3 image in Fig. 6b.

It should be noted that the wire-like diamond aggregates observed in Fig. 6a are actually of plate-like geometry that was investigated by the tilting experiments in TEM (not shown here). Briefly, the tilting experiments indicated that when (i) the samples were tilted around an axis in perpendicular to the DNW (such as the *x*-axis designated in Fig. 6b), the image of the diamond clusters remained about the same length with the same dark contrast, but when (ii) the samples were tilted around an axis in parallel with the DNW (such as the *y*-axis designated in Fig. 6b), the image of the diamond clusters slightly increased in width and gradually disappeared. This observation implies that the DNW structure shown in the TEM micrograph in Fig. 6b is the edge-on image of a plate-like diamond aggregate.

The true shape of the diamond aggregate in DNW_0 is like the one schematically shown in Fig. 6c, *viz.* it contains parallel stacking of (111) diamond lattice planes with a few graphitic layers, sitting on the top of the surface (Fig. $6c_I$). The ambiguity in the interpretation of the geometry of the DNW structure from its TEM micrograph comes from the phenomenon that the diamond aggregates were observable only when they were oriented with $[1\bar{1}0]$ of diamond grains aligned in parallel with the electron beams, *i.e.*, oriented in $[10\bar{1}]$ zone axis (Z. A.). In this orientation, the {111} lattice planes of diamond are parallel with the electron beam and diffract the electrons strongly,

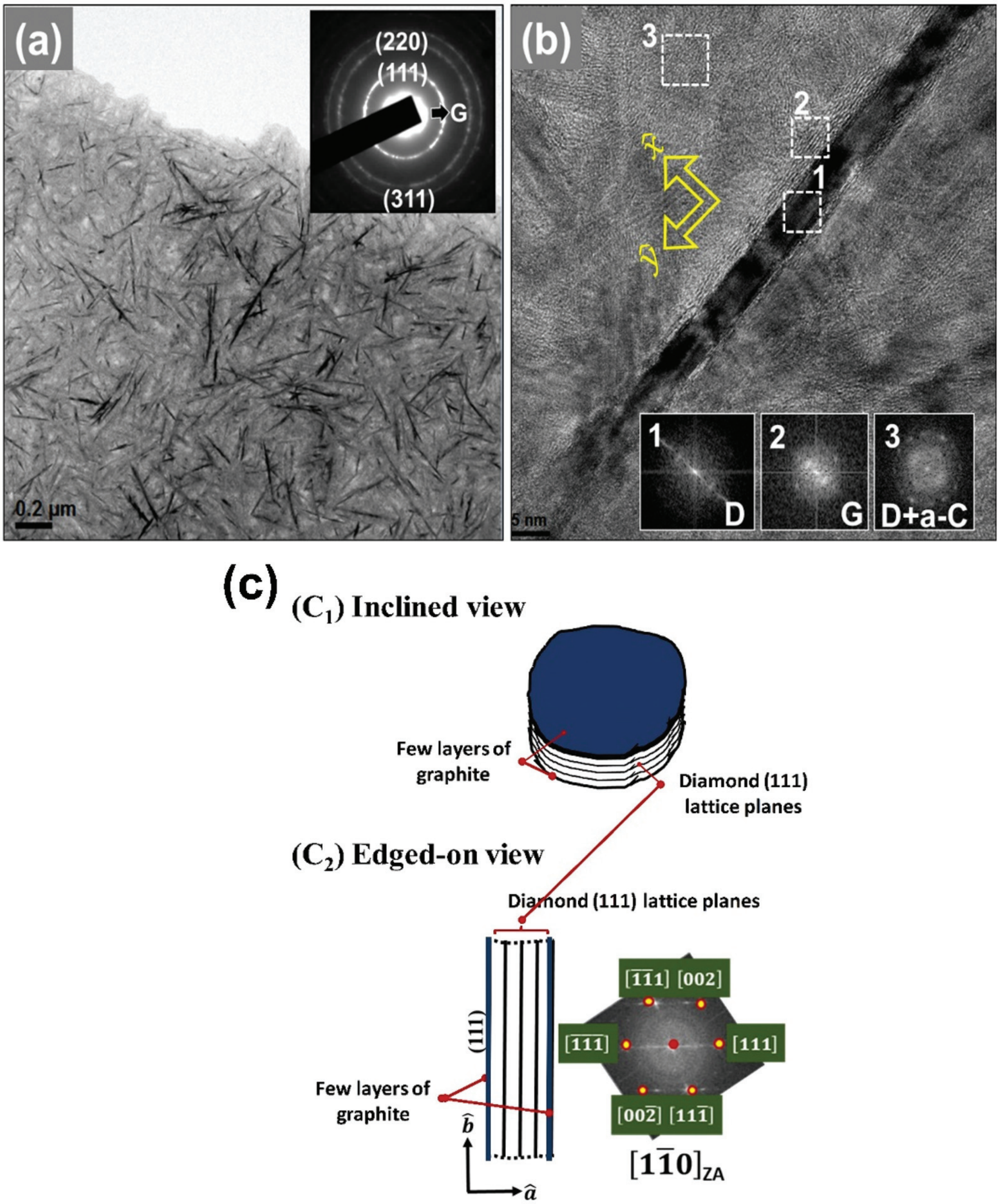

Fig. 6 TEM analysis of the pristine DNW films. (a) Bright-field TEM image of DNW$_0$ with inset SAED pattern showing the (311), (220), and (111) diffraction rings of diamond. (b) High-resolution TEM image clearly showing the nanowire structure with a diamond phase encapsulated by a graphitic phase. Inset FT images show the phase content at the respective marked areas. (c) The schematic of the plate-like geometry of the diamond aggregates in DNW$_0$, where (c$_{\rm I}$) shows the inclined view and (c$_{\rm II}$) shows the edged-on view of the plate-like diamond aggregates.

resulting in dark contrast for the diamond aggregates. The {111} lattice planes of diamond are seen as parallel fringes with an interplanar spacing of d_{111} = 0.21 nm (*cf.* Fig. 6b). When the diamond samples were aligned in other Z. A., such as [001] or [111], the lattice planes aligned in parallel with electron beams will be the {100} families or the aligned [111] Z. A., where the lattice planes in parallel with the electron beams will be $\{10\bar{1}\}$ families. These lattice planes have interplanar spacings of d_{400} = 0.09 nm and d_{202} = 0.12 nm, which are too small to be resolvable by TEM, as the resolution limit of a conventional TEM is d_s = 0.18 nm. The diamond aggregates oriented in these non-$[10\bar{1}]$ zone axes diffract electrons inefficiently and the images of the aggregates look like gray contrast (thickness contrast), which is difficult to resolve from the background matrix of amorphous materials.

The hydrogenation process has a significant effect on the microstructure of the DNW$_0$ films. As experimentally observed with TEM in Fig. 7a, a plate-like geometry with a shorter diameter and thicker thickness was recorded for the DNW$_{10}$ films in comparison with the plate-like structure for the DNW$_0$ films shown in Fig. 6a. This result is consistent with the morphology seen in the FESEM images in Fig. 1c. Moreover, the appear-

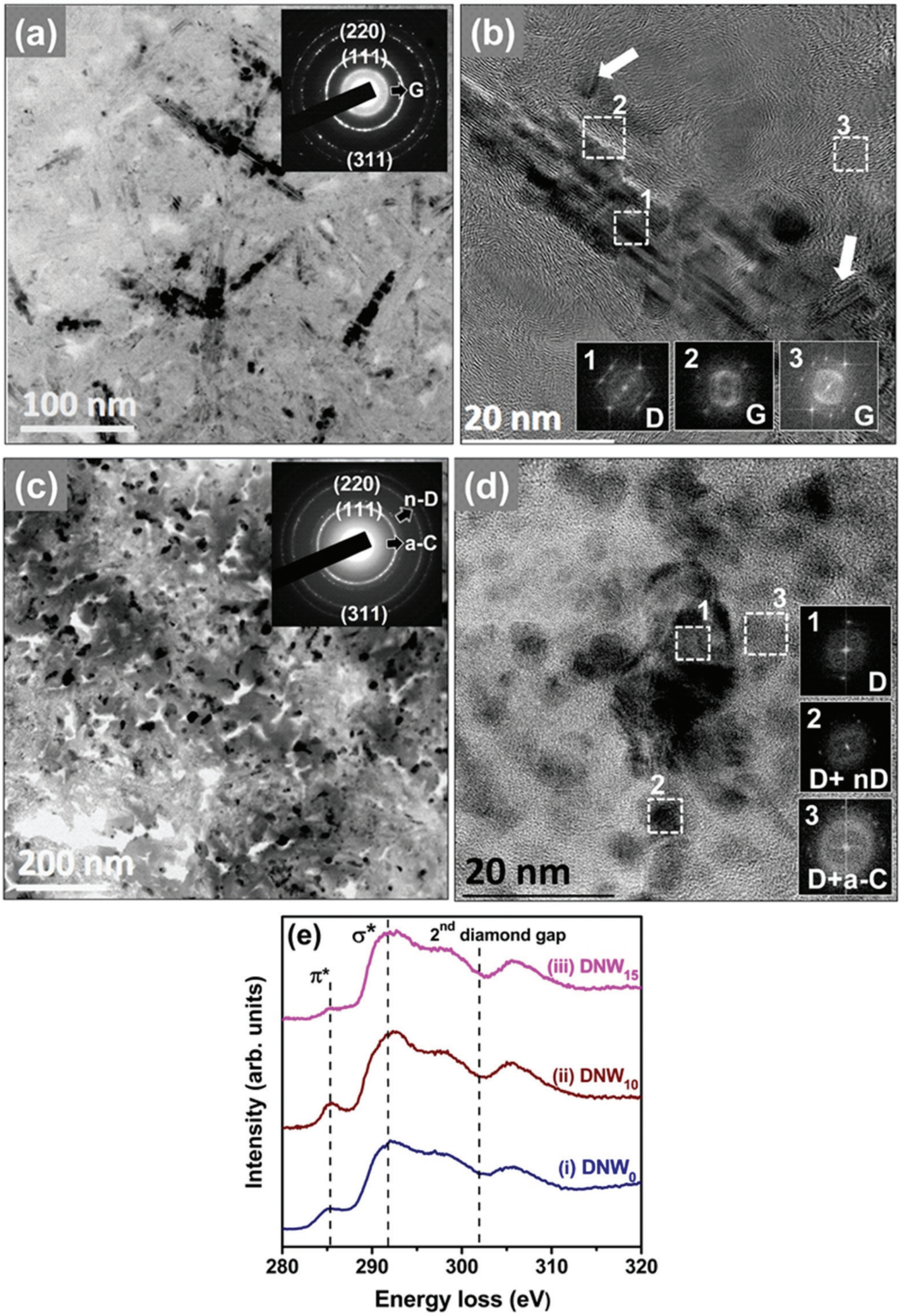

Fig. 7 TEM analysis of the hydrogenated DNW films (a) TEM image of the DNW_{10} film with the inset showing the SAED pattern. (b) High-resolution TEM image with inset FT images show the phase content of the respective marked areas. (c) TEM image of the DNW_{15} films with the inset showing the SAED pattern. (d) High-resolution TEM image of the DNW_{15} showing the absence of the nanowire morphology due to the hydrogenation process. The phase content of the respective marked areas is shown in the inset. (e) EELS spectra of (i) DNW (DNW_0) and (ii and iii) hydrogenated DNWs: (ii) DNW_{10} and (iii) DNW_{15} films.

ance of a spotty SAED pattern for the DNW_{10} films shown in the inset of Fig. 7a indicates a better crystalline ordered diamond phase in contrast to the pristine DNW_0 films (Fig. 6a). The FT_1 image corresponding to region 1 in Fig. 7b reveals the diamond structure of the DNWs. FT images (FT_2) corresponding to region 2 in Fig. 7b reveal dumbbell-like diffraction spots, indicating the presence of graphitic structures. Furthermore, the plate-like diamond aggregates in DNW$_0$ appear to disintegrate into shorter and thinner segments in DNW$_{10}$ films by the hydrogen plasma, as marked by the arrows in Fig. 7b. Most of the regions surrounding the DNW$_0$ were transformed from a nanocarbon phase (diamond + a-C) to a graphitic phase by the hydrogenation process. In contrast, the plate-like granular structure of the pristine DNW$_0$ films could not be observed when the films were subjected to extended hydrogenation periods, as shown in the BF TEM image in Fig. 7c for the DNW$_{15}$ films. The corresponding SAED pattern shown in the inset of Fig. 7c reveals the presence of the (311), (220), and (111) diffraction rings, as in the DNW$_0$ film (*cf.* Fig. 6a), indicating that the diamond structure of the DNW$_{15}$ is preserved. However, the diffused ring in the center of the SAED pattern is blurred, indicating the transformation of the graphitic phase into the a-C phase due to the longer hydrogenation treatment. The corresponding HRTEM image in Fig. 7d clearly shows the presence of nanosized diamond grains of 5 to 10 nm. Interestingly, the plate-like aggregates seen in Fig. 6a have completely disappeared and a blurry a-C phase appeared in Fig. 7c. The FT images (FT$_1$–FT$_3$), corresponding to regions 1–3 marked in the inset in Fig. 7d, reveal the presence of a-C phases with a small proportion of diamond. Therefore, it can be concluded that the graphitic phase around and throughout the DNW$_{10}$ films has completely transformed to nano-sized diamond with an a-C phase, due to the prolonged hydrogenation effect. Moreover, the TEM results for the DNW$_{15}$ films agree well with the Raman results, which show a red-shift of the D* and G peaks that indicate the transformation of the sp^2 graphitic phases into a-C phases (*cf.* Fig. 1e, iv).

Selective area electron energy loss spectroscopy (EELS) spectra were recorded in the carbon K-edge region to explicitly differentiate between the different carbon materials (*e.g.*, diamond, graphite, and a-C phases) contained in the DNW$_0$, DNW$_{10}$ and DNW$_{15}$ films (Fig. 7e).[63,64] The weak peak around 285.1 eV (the π*-band) in spectrum i in Fig. 7e for the DNW$_0$ films indicates the presence of a small fraction of the sp^2 phase. Interestingly, the π*-band intensity improved significantly for DNW$_{10}$ (spectrum ii, Fig. 7e), indicating the presence of improved graphitic phase fractions. However, a small signal near 285.1 eV (spectrum iii, Fig. 7e) indicates the etching of the graphitic phase from the DNW$_{15}$ surface. Both the TEM and EELS observations suggest that hydrogenation for a short period markedly increased the metallic sp^2 nanographitic phase fractions; however, extended hydrogenation etched the graphitic phase content from the surface.

4. Discussion

The major difference between the pristine (DNW$_0$) and hydrogenated DNWs (DNW$_5$, DNW$_{10}$ and DNW$_{15}$) is the modification of their respective microstructure and chemical structures caused by the hydrogenation process, as revealed by the Raman, XPS and TEM measurements. The Raman spectra indicate the formation of disordered carbon and sp^2 nanographitic phases in DNW$_5$ and DNW$_{10}$ films, as shown in Fig. 1e spectra ii and iii, respectively, while an extended hydrogenation processing (*i.e.* DNW$_{15}$, Fig. 1e, spectrum iv) etches the nanographitic phases from the surface. Furthermore, the XPS spectra show the formation of a graphitic phase for the DNW$_5$ and DNW$_{10}$ in Fig. 1f spectra ii and iii, respectively; however, extended hydrogenation etches the graphitic phase from the DNW$_{15}$ surfaces as shown in Fig. 1f spectra ii. The Raman and XPS results complement each other well.

Restated, both the Raman and XPS measurements indicate the induction of increased sp^2 nanographitic phases in DNW$_5$ and DNW$_{10}$ films. The change in the chemical microstructure and phase can play a role in the effective charge trapping for hydrogenated DNW films. The hydrogenated DNW$_5$ and DNW$_{10}$ films have better conducting nanographitic sp^2 phase fractions than the pristine DNW$_0$ films. The presence of these metallic nanographitic phases embedded in the diamond matrix makes them unable to serve as electron trap centers, as the electron charges will be dissipated without any dielectric support for trapping these charges.[65–67] Kawanami *et al.* reported enhanced charge storage properties and a threshold voltage shift with the presence of metallic cobalt and cobalt silicide in a dielectric SiO$_2$ thin film matrix.[68] Hattori *et al.* demonstrated enhanced charge-trapping properties of different sizes of Au nanoparticles embedded in p- and n-doped Si substrates.[69] Furthermore, the presence of foreign metal nanocrystals (*e.g.* Au, Ag, and Pt) in thin SiO$_2$ films has improved the charge-trapping properties and charge retention times for nonvolatile memory applications.[70–72] In addition to the enhanced charge-trapping properties of metallic nanoclusters embedded in a dielectric material, stable defect sites in the hydrogenated DNW caused by a hydrogen plasma treatment can act as charge-trapping centers.[73,74] Thus, a nonconducting support is necessary, in addition to the presence of a metallic nanographitic phase, for these DNWs to serve as superior charge trapping materials. The formation of the plate-like diamond aggregates, as observed from TEM experiments (schematically explained in Fig. 8), forming nanosized diamond-graphite clusters (DGCs), serves as an ideal metallic and dielectric pair for trapping the charges.

The presence of the DGCs can also account for the increased charge-trapping properties of the pristine DNW$_0$ as the hydrogenation period is extended to 5 and 10 minutes. The possible explanation is that, as the hydrogenation period is increased, the disintegration of the DGCs starts to appear on the DNW surface.[75,76] The disintegration in the DGC morphologies was directly observed during the TEM (Fig. 7) as well as SEM measurements (Fig. 1(a)–(d)). Moreover, the Raman spectra reveal a broadened D* peak with red shifting of G peaks for the DNW$_5$ and DNW$_{10}$ films (Fig. 1e, spectra ii and iii) compared with the DNW$_0$ film (Fig. 1e, spectrum i), indicating the presence of defect sites in the hydrogenated DNW$_5$ and DNW$_{10}$ films.[45] These defect sites can help in trapping the charge easily, because their presence lowers the mobility of

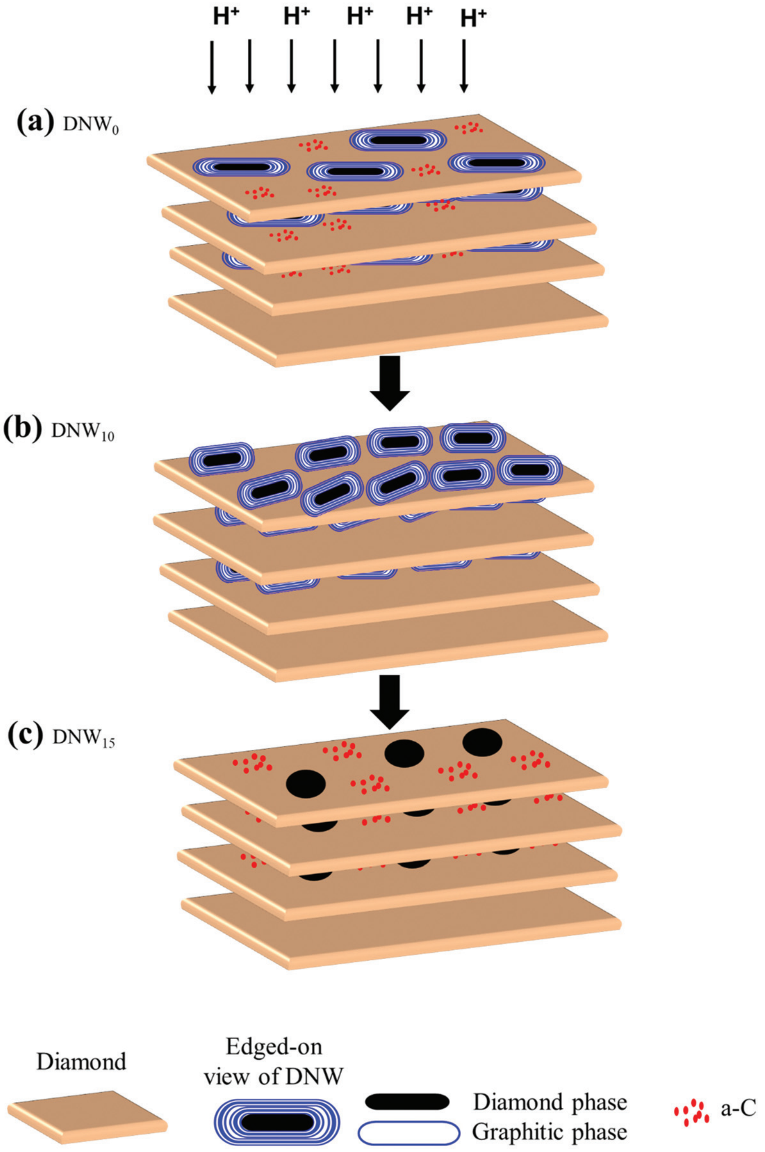

Fig. 8 Schematic representation showing the hydrogen plasma effect on the microstructure of DNW films (a) DNW_0, (b) DNW_{10} and (c) DNW_{15} films.

electrons *via* the impurity scattering mechanism and lowers the conductivity of the materials by decreasing the electron concentrations.[73,74] Furthermore, XPS results (Fig. 1f, spectra ii and iii) show the C 1s peak shifting towards a lower binding energy (*i.e.*, the graphitic side) with respect to the hydrogenation period indicating the formation of abundant nanographitic phases in DGCs on the DNW_5 and DNW_{10} surfaces. However, with the extended hydrogenation period, the C 1s shifts towards a higher binding energy (Fig. 1f, spectra ii and iii), indicating the etching of the ordered nanographitic phases *i.e.* DGCs (transformation from sp^2 nanographitic to a diamond or a-C phase). This change in the chemical structure of these DNWs due to the hydrogenation process seems to have a significant effect on the enhanced/degraded charge-trapping properties, respectively. Furthermore, the Raman and XPS results are well supported by the TEM observations described in Fig. 6 and 7. TEM Fourier transform image investigations (Fig. 7b) revealed the presence of a nanographitic sp^2 phase throughout the DNW_{10} surface in comparison with the DNW_0 (Fig. 6b) or DNW_{15} (Fig. 7d) surfaces. Again, this fact is supported by the EELS measurement shown in Fig. 7e. The presence of the peak around 285.1 eV indicates the presence of a more sp^2 nanographitic phase in the DNW_{10} surface (Fig. 7e, spectrum II) compared with DNW_0 (Fig. 7e, spectrum I) or DNW_{15} (Fig. 7e, spectrum III). Initially, the charge storage properties of DNW_5 and DNW_{10} materials increased as the hydrogenation period increased because of the availability of increased charge-trapping sites (*i.e.*, the DGCs). However, the extended hydrogenation period of the DNW films (*i.e.*, the DNW_{15} in Fig. 7d) resulted in the etching of the DGCs from the surface, which starts to degrade the charge-trapping properties.

For better understanding the effect of the hydrogenation process on the microstructure of the DNW films, Fig. 8 is schematically illustrated. The pristine DNW_0 surfaces consist of parallelly stacked (111) diamond lattice plates with diamond structures in the form of DGCs with graphite and plate-like diamond aggregates (*cf.* TEM micrograph in Fig. 6b). The diamond structures in DNW_0 (filled black oval in Fig. 8a) are relatively large, ∼50–200 nm and possess a medium level of charge trapping ability. These DNWs were surrounded by a matrix of amorphous carbons (red dots in Fig. 8a), with little conductivity, acting as the leaking path for trapped charges. It should be noted that the hydrogenation process alters the physiochemical properties of the topmost layers of the DNWs. With respect to the hydrogenation period, the length of the DGCs was shorter (length of $DNW_0 > DNW_5 > DNW_{10}$ as observed from the SEM image in Fig. 1 and TEM structure image in Fig. 6b and 7b, d), and the phase fraction of the DGCs increases ($DNW_0 < DNW_5 < DNW_{10}$). A short time hydrogenation process, as in the case of DNW_{10}, yields abundant DGCs, thereby enhancing the volume fraction of the nanographitic phase on the DNW_{10} surface. Moreover, the interlayer a-C phase between the few topmost layers transforms to nanographitic by the hydrogenation process. These nanographite aggregates act as perfect local charge trapping centers.[65–70] Moreover, the local charge trapping at the defect sites created by the aggressive hydrogen plasma further boosts the overall charge-trapping on the hydrogenated DNW_{10} surface. However, when these DNWs were hydrogenated for an extended period (Fig. 8c) *i.e.* DNW_{15}, the DGCs on the surface were completely etched away and thereby lost the charge-trapping ability.

The presented results show the modification of charge-trapping properties of DNW materials with high spatial resolution due to the hydrogenation process, which allows for practical applications of DNW materials in nanotechnology. Moreover, the charge trapping properties of the DNW materials are believed to vary with the different diamond microstructures, chemical constituents, and different surface treatment procedures. The induced potential contrast corresponds mostly to charges trapped inside the DNW films, which persist for a long time even after the charging. Such a behavior paves the way for the real applications of these hydrogenated DNWs for diamond-based electronic devices. The directed nano-assemblies of biomolecules or colloidal nanoparticles on the patterned charged areas on DNW materials are promising building blocks for emerging nanotechnology applications including chemical and biological sensing, nanoelectronics, and optoelectronics.[77–79] Moreover, hydrogenation induced effective charge-trapping and the role of DGC could provide a strategy for further enhancing charge trapping properties in diamond-based charge storage devices. This study opens up new directions for the charge trapping properties of other carbon-based nanomaterials by tuning the sp^2/sp^3 phase fractions and various defect states, which will be the new methods for charge-trapping layers in charge-trap flash memory devices.

5. Conclusion

In summary, charge injection into DNW surfaces can be well controlled by the external bias and applied load of an AFM tip. Both positive and negative charges can be stored in nanometer-scale patterns with different shapes and sizes on the DNW surfaces. A simple hydrogen plasma treatment of appropriate duration (DNW_{10}) is observed to effectively enhance the charge-trapping properties of these DNWs. The enhanced charge-trapping properties of hydrogenated DNWs are attributed to the formation of plate-like diamond-graphite nanocomposites of higher phase fractions. Abundant plate-like diamond-graphite nanocomposites in a dielectric diamond matrix are observed to trap more charges, which can be used for battery applications. Moreover, we believe that these results are significant and of wide interest in the field of nanoscience, especially in the triboelectric nanogenerator application field, because of the potential of a simple hydrogenation process on effective charge-trapping properties for diamond and other nanocarbon based materials.

Conflicts of interest

There are no conflicts to declare.

Acknowledgements

This work was supported by the Institute for Basic Science (IBS) [IBS-R004] and by the European Commission under the project, QUEFORMAL [829035] and Graphene Flagship [881603].

References

1 M. L. Juan, M. Righini and R. Quidant, *Nat. Photonics*, 2011, **5**, 349–356.
2 D. Erickson, X. Serey, Y. F. Chen and S. Mandal, *Lab Chip*, 2011, **11**, 995–1009.
3 Y. Pang and R. Gordon, *Nano Lett.*, 2012, **12**, 402–406.
4 M. L. Juan, R. Gordon, Y. Pang, F. Efterkhari and R. Quidant, *Nat. Phys.*, 2009, **5**, 915–919.
5 P. Calvert, *Chem. Mater.*, 2001, **13**, 3299–3305.
6 C. Zhang, W. Tang, L. Zhang, C. Han and Z. L. Wang, *ACS Nano*, 2014, **8**, 8702–8709.
7 R. V. Dommelen, P. Fanzio and L. Sasso, *Adv. Colloid Interface Sci.*, 2018, **251**, 97–114.
8 S. D. Tzeng, K. J. Lin, J. C. Hu, L. J. Chen and S. Gwo, *Adv. Mater.*, 2006, **18**, 1147–1151.
9 H. Fudouzi, M. Kobayashi and N. Shinya, *J. Nanopart. Res.*, 2001, **3**, 193–200.

10 L. J. Guo, *Adv. Mater.*, 2007, **19**, 495–513.

11 D. Zhao, L. Duan, M. Xue, W. Ni and T. Cao, *Angew. Chem., Int. Ed.*, 2009, **48**, 6699–6703.

12 X. Ma, D. Zhao, M. Xue, H. Wang and T. Cao, *Angew. Chem., Int. Ed.*, 2010, **49**, 5537–5540.

13 H. O. Jacobs and G. M. Whitesides, *Science*, 2001, **291**, 1763–1766.

14 H. O. Jacobs, S. A. Campbell and M. G. Steward, *Adv. Mater.*, 2002, **14**, 1553–1557.

15 C. R. Barry and H. O. Jacobs, *Nano Lett.*, 2006, **6**, 2790–2796.

16 J. J. Cole, C. R. Barry, X. Wang and H. O. Jacobs, *ACS Nano*, 2010, **4**, 7492–7498.

17 J. W. Jeong, W. I. Park, L. M. Do, J. H. Park, T. H. Kim, G. Chae and Y. S. Jung, *Adv. Mater.*, 2012, **24**, 3526–3531.

18 Y. S. Jung, W. Jung, H. L. Tuller and C. A. Ross, *Nano Lett.*, 2008, **8**, 3776–3780.

19 J. E. Stern, B. D. Terris, H. J. Mamin and D. Rugar, *Appl. Phys. Lett.*, 1988, **53**, 2717–2719.

20 M. K. Mazumder, S. Banerjee, R. E. Ware, C. Mu, N. Kaya and C. C. Huang, *IEEE Trans. Ind. Appl.*, 1994, **30**, 365–369.

21 W. Kleber and B. Makin, *Part. Sci. Technol.*, 1998, **16**, 43–53.

22 B. A. Kwetkus, *Part. Sci. Technol.*, 1998, **16**, 1655–1668.

23 F. R. Fan, Z. Q. Tian and Z. L. Wang, *Nano Energy*, 2012, **1**, 328–334.

24 F. R. Fan, L. Lin, G. Zhu, W. Z. Wu, R. Zhang and Z. L. Wang, *Nano Lett.*, 2012, **12**, 3109–3114.

25 S. H. Wang, L. Lin and Z. L. Wang, *Nano Lett.*, 2012, **12**, 6339–6346.

26 Y. Yang, H. L. Zhang, J. Chen, Q. S. Jing, Y. S. Zhou, X. N. Wen and Z. L. Wang, *ACS Nano*, 2013, **7**, 7342–7351.

27 S. H. Wang, L. Lin, Y. N. Xie, Q. S. Jing, S. M. Niu and Z. L. Wang, *Nano Lett.*, 2013, **13**, 2226–2233.

28 L. Lin, S. H. Wang, Y. N. Xie, Q. S. Jing, S. M. Niu, Y. F. Hu and Z. L. Wang, *Nano Lett.*, 2013, **13**, 2916–2923.

29 S. M. Niu, Y. Liu, S. H. Wang, L. Lin, Y. S. Zhou, Y. F. Hu and Z. L. Wang, *Adv. Mater.*, 2013, **25**, 6184–6193.

30 G. Zhu, Z. H. Lin, Q. S. Jing, P. Bai, C. F. Pan, Y. Yang, Y. S. Zhou and Z. L. Wang, *Nano Lett.*, 2013, **13**, 847–853.

31 (*a*) C. Chappert, A. Fert and F. N. Van Dau, *Nat. Mater.*, 2007, **6**, 813–823; (*b*) M. Wuttig and N. Yamada, *Nat. Mater.*, 2007, **6**, 824–832; (*c*) R. Waser and M. Aono, *Nat. Mater.*, 2007, **6**, 833–840; (*d*) W. Lu and C. M. Lieber, *Nat. Mater.*, 2007, **6**, 841–850.

32 (*a*) Y. Wang, X. Q. Zhou, B. C. Chen and Q. Zhang, *IEEE Trans. Dielectr. Electr. Insul.*, 2010, **17**, 1036–1042; (*b*) V. K. Thakur and R. K. Gupta, *Chem. Rev.*, 2016, **116**, 4260–4317.

33 C. Lee, J. H. Kwon, J. S. Lee, Y. M. Kim, Y. Choi, H. Shin, J. Lee and B. H. Sohn, *Appl. Phys. Lett.*, 2007, **91**, 153506–153509.

34 J. S. Lee, J. Cho, C. Lee, I. Kim, J. Park, Y. M. Kim, H. Shin, J. Lee and F. Caruso, *Nat. Nanotechnol.*, 2007, **2**, 790–795.

35 H. Jacobs and A. Stemmer, *Surf. Interface Anal.*, 1999, **27**, 361–367.

36 T. Itoh, T. Ito, H. Kuriyama and S. Nonomura, *Jpn. J. Appl. Phys.*, 2016, **55**, 04ES13–04ES19.

37 N. Naujoks and A. Stemmer, *Microelectron. Eng.*, 2005, **78/79**, 331–337.

38 Y. G. Feng, Y. B. Zheng, G. Zhang, D. A. Wang, F. Zhou and M. W. Liu, *Nano Energy*, 2017, **38**, 467–476.

39 K. J. Sankaran, M. Ficek, K. Panda, C. J. Yeh, M. Sawczak, J. Ryl, K. C. Leou, J. Y. Park, I. N. Lin, R. Bogdanowicz and K. Haenen, *ACS Appl. Mater. Interfaces*, 2019, **11/51**, 48612–48623.

40 K. Panda, B. Sundaravel, B. K. Panigrahi, P. Magudapathy, D. N. Krishna, K. G. M. Nair, H. C. Chen and I. N. Lin, *J. Appl. Phys.*, 2011, **110**, 044304–044313.

41 Y. Xie, C. Bell, C. Yajima, Y. Hikita and H. Y. Hwang, *Nano Lett.*, 2010, **10**, 2588–2591.

42 K. J. Sankaran, J. Kurian, H. C. Chen, C. L. Dong, C. Y. Lee, N. H. Tai and I. N. Lin, *J. Phys. D: Appl. Phys.*, 2012, **45**, 365303–365313.

43 T. M. Babinec, B. J. M. Hausmann, M. Khan, Y. Zhang, R. J. Maze, P. R. Hemmer and A. Lončar, *Nat. Nanotechnol.*, 2010, **5**, 195–199.

44 K. Panda, N. Kumar, K. J. Sankaran, B. K. Panigrahi, S. Dash, H. C. Chen, I. N. Lin, N. H. Tai and A. K. Tyagi, *Surf. Coat. Technol.*, 2012, **207**, 535–545.

45 A. C. Ferrari and J. Robertson, *Phys. Rev. B: Condens. Matter Mater. Phys.*, 2000, **61**, 14095–14107.

46 K. Panda, K. J. Sankaran, B. K. Panigrahi, N. H. Tai and I. N. Lin, *ACS Appl. Mater. Interfaces*, 2014, **6**, 8531–8541.

47 Y. Taki and O. Takai, *Thin Solid Films*, 1998, **316**, 45–50.

48 P. A. Bruhwiler, A. J. Maxwell, C. Puglia, A. Nilsson, S. Andersson and N. M. Artensson, *Phys. Rev. Lett.*, 1995, **74**, 614–617.

49 J. F. Morar, F. J. Himpsel, G. J. Hollinger, L. Jordan, G. Hughes and F. R. McFeely, *Phys. Rev. B: Condens. Matter Mater. Phys.*, 1986, **33**, 1340–1345.

50 J. Diaz, G. Paolicelli, S. Ferrer and F. Comin, *Phys. Rev. B: Condens. Matter Mater. Phys.*, 1996, **54**, 8064–8069.

51 J. Y. Park, S. Maier, B. Hendriksen and M. Salmeron, *Mater. Today*, 2010, **13**, 38–45.

52 J. Ha, J. Chung, S. M. Kim, J. H. Kim, S. Shin, J. Y. Park, S. Lee and J. B. Kim, *Nano Energy*, 2017, **36**, 126–133.

53 K. Panda, J.-E. Kim and J. Y. Park, *Carbon*, 2019, **141**, 123–133.

54 J. H. Kim, B. K. Yun, J. H. Jung and J. Y. Park, *Appl. Phys. Lett.*, 2016, **108**, 133901–133906.

55 E. Palleau, L. Ressier, Z. Borowik and T. Melin, *Nanotechnology*, 2010, **21**, 225706–225713.

56 H. Sugimura, Y. Ishida, K. Hayashi and O. Takai, *Appl. Phys. Lett.*, 2002, **80**, 1459–1461.

57 T. Konig, G. H. Simon, L. Heinke, L. Lichtenstein and M. Heyde, *Beilstein J. Nanotechnol.*, 2011, **2**, 1–14.

58 Y. Zhang, D. Ziegler and M. Salmeron, *ACS Nano*, 2013, **7**, 8258–8265.

59 C. Nebel, *Semicond. Sci. Technol.*, 2003, **18**, S1–S11.

60 F. Maier, M. Riedel, B. Mantel, J. Ristein and L. Ley, *Phys. Rev. Lett.*, 2000, **85**, 3472–3475.

61 P. Mesquida and A. Stemmer, *Adv. Mater.*, 2001, **13**, 1395–1398.

62 J. Y. Park and M. Salmeron, *Chem. Rev.*, 2014, **114**, 677–711.

63 A. Dato, V. Radmilovic, Z. Lee, J. Philips and M. Frenklach, *Nano Lett.*, 2008, **8**, 2012–2016.

64 P. K. Chu and L. Li, *Mater. Chem. Phys.*, 2006, **96**, 253–277.

65 Z. Liu, C. Lee, V. Narayanan, G. Pei and E. C. Kan, *IEEE Trans. Electron Devices*, 2002, **49**, 1614–1622.

66 M. Takata, S. Kondoh, T. Sakaguchi, H. Choi, J.-C. Shim, H. Kurino and M. Koyanagi, *IEDM Tech. Dig.*, 2003, **10**, 553–556.

67 P. Kervalishvili and A. Lagutin, *Microelectron. J.*, 2008, **39**, 1060–1065.

68 A. K. Kawanami, M. M. Ikeda and S. Miyazaki, *Jpn. J. Appl. Phys.*, 2010, **49**, 08JA04–08JA08.

69 S. Hattori, M. Terai and H. Nishizawa, *Jpn. J. Appl. Phys.*, 2016, **55**, 025002–025009.

70 C. Lee, J. Meteer, V. Narayanan and C. E. Kan, *J. Electron. Mater.*, 2005, **34**, 1–11.

71 B. K. Park, C. H. Kim and S. Kim, *Semicond. Sci. Technol.*, 2006, **21**, 975–978.

72 C. J. Park, K. H. Cho, W. C. Yang, H. Y. Cho, S. H. Choi, R. G. Elliman, J. H. Han and C. Kim, *Appl. Phys. Lett.*, 2006, **88**, 071916–071919.

73 R. Kressmann, G. M. Sessler and P. Günther, *IEEE Trans. Dielectr. Electr. Insul.*, 1996, **3**, 607–623.

74 S. M. Sze, *Physics of Semiconductor Devices*, Wiley & Sons, New York, 1981, p. 394.

75 Y. Yamazakia, K. Ishikawa, S. Samukawa and S. Yamasaki, *Physica B*, 2006, **376**/**377**, 327–330.

76 Y. Yamazaki, K. Ishikawa, N. Mizuochi and S. Yamasaki, *Diamond Relat. Mater.*, 2005, **14**, 1939–1942.

77 M. Lions, S. Saada, B. Bazin, M.-A. Pinault, F. Jomard, F. Andrieu, O. Faynot and P. Bergonzo, *Diamond Relat. Mater.*, 2010, **19**, 413–417.

78 H. A. Girard, S. Perruchas, C. Gesset, M. Chaigneau, L. Vieille, J.-C. Arnault, P. Bergonzo, J.-P. Boilot and T. Gacoin, *ACS Appl. Mater. Interfaces*, 2009, **1**, 2738–2746.

79 W. Dexters, E. Bourgeois, M. Nesládek, J. D'Haen, E. Goovaerts and K. Haenen, *Phys. Chem. Chem. Phys.*, 2015, **17**/**15**, 9619–9623.